Wang *et al. Journal of Nanobiotechnology* (2025) 23:234
https://doi.org/10.1186/s12951-025-03290-5

Journal of Nanobiotechnology

RESEARCH **Open Access**

Microalgae-based biodegradable embolic agent for the treatment of hepatocellular carcinoma through transarterial embolization

Kaiyue Wang[1†], Danni Zhong[2†], Lingxiao Yang[4†], Cheng Zeng[1], Qitao Hu[1], Min Zhou[1,2,3,5,6*] and Zhe Tang[1,7*]

Abstract

Transarterial chemoembolization (TACE) serves as a locoregional therapy for hepatocellular carcinoma (HCC) patients. Nevertheless, the rapid dissociation of conventional TACE (cTACE) preparations, attributed to the instability of the emulsion, often leads to inadequate concentrations of chemotherapeutic agents within the tumor site. Consequently, there exists a pressing demand for an embolic agent that possesses facile injectability and the capacity to provide continuous delivery of chemotherapy drugs. Herein, we leveraged the inherent drug-loading capabilities and distinctive structural attributes of *Spirulina platensis* (SP) to formulate a novel microalgae embolic agent, doxorubicin loaded-*Spirulina platensis* (DOX-SP). The DOX-SP formulation exhibited a notable capacity for drug loading and demonstrated the ability to sustain drug release in response to acidic tumor microenvironments (TME). The spiral structure and micron-scale size of SP contributed to effective vascular embolization and continuous localized release of DOX. Furthermore, the biodegradability of SP as a natural biomaterial ensured good biosafety, with its degradation products potentially enhancing the pH of TME. In a rat model of in-situ hepatocellular carcinoma, DOX-SP effectively suppressed tumor growth and significantly reduced tumor size following intra-arterial injection, while exhibiting minimal adverse effects. Taken together, the high drug loading capacity, effective vascular embolization, pH sensitivity, TME pH modulation, and biodegradability of DOX-SP made it a promising embolic agent for hepatocellular carcinoma treatment.

Keywords Liver cancer, Drug delivery, Microalgae, Transarterial embolization, Biodegradable

---

†Kaiyue Wang, Danni Zhong and Lingxiao Yang contributed equally to this work.

*Correspondence:
Min Zhou
zhoum@zju.edu.cn
Zhe Tang
8xi@zju.edu.cn
[1]Department of Surgery, Center for Cancer Medicine, the Fourth Affiliated Hospital of School of Medicine, and International School of Medicine, International Institutes of Medicine, Zhejiang University, Yiwu 322000, China
[2]Zhejiang University-University of Edinburgh Institute (ZJU-UoE Institute), Zhejiang University School of Medicine, Zhejiang University, Haining 314400, China
[3]Key Laboratory of Cancer Prevention and Intervention (Ministry of Education), Zhejiang University, Hangzhou 310009, China
[4]Department of Respiratory and Critical Care Medicine, the Fourth Affiliated Hospital of School of Medicine, and International School of Medicine, International Institutes of Medicine, Zhejiang University, Yiwu 322000, China
[5]Zhejiang University-Ordos City Etuoke Banner Joint Research Center, Zhejiang University, Haining 314400, China
[6]The National Key Laboratory of Biobased Transportation Fuel Technology, Zhejiang University, Hangzhou 310027, China
[7]Department of Surgery, The Second Affiliated Hospital, Zhejiang University School of Medicine, Hangzhou, China

Introduction

Hepatocellular carcinoma (HCC) is the sixth most common malignancy worldwide and the third leading cause of cancer-related death [1], attributed to its complex oncogenesis, recurrence, and metastasis [2]. Multiple therapeutic approaches, including localized treatment, liver transplantation, surgical resection and systemic therapy, are available for HCC management [3]. However, approximately 70% of patients are diagnosed at an advanced stage due to early-stage HCC's asymptomatic nature [4], limiting opportunities for surgical tumor removal. Transarterial chemoembolization (TACE) is a recommended treatment for intermediate to advanced-stage HCC [5]. The use of TACE improves overall survival in patients with unresectable, non-metastatic hepatocellular carcinoma [6]. The unique vascular characteristics of HCC render TACE a safe and promising treatment option. There are typically two forms of TACE: conventional TACE (cTACE) and drug-eluting bead TACE (DEB-TACE) [7]. cTACE employs lipiodol (LPD) and chemotherapy drug emulsion. LPD exhibits instantaneous and malleable embolic effects, enhancing the localized delivery of drugs to HCC. However, this emulsion is unstable, which typically exhibits poor physical stability and rapid phase separation. This results in suboptimal embolization strength, swift metabolic processing in the body, and less than ideal release of the chemotherapy drug.

The efficacy of the LPD system is constrained by its characteristic of rapid drug release. This rapid release of the chemotherapy drug in a short timeframe heightens the risk of systemic toxicity and diminishes the therapeutic effect [8]. Additionally, inconsistent embolization can lead to incomplete tumor necrosis and increase the chances of recurrence. Presently, DEB-TACE is widely used in clinical practice. Typically, these microspheres are loaded with chemotherapeutic agents such as Doxorubicin (DOX) and irinotecan [9]. Some clinical studies indicate that compared to conventional cTACE, DEB-TACE offers a superior objective response, disease control, and a lower risk of complications [10]. However, other studies suggest that both techniques demonstrate comparable overall survival rates and disease control [7]. Janek et al. compared acrylamido-polyvinylalcohol-AMPS hydrogel microspheres and polyvinyl alcohol-co-acrylic acid microspheres for unresectable HCC, results showed no significant differences in survival [11]. Developing an efficient embolizing agent remains a challenge and improvements in embolic materials could offer significant clinical benefits. Early embolic materials included autologous blood clots and gelatin sponges [12]. However, due to their unpredictable size and shape, the risk of non-target embolization was high. Common DEB-TACE products, such as DC Bead, Callisphere, and HepaSphere, are non-degradable microspheres. Calibrated microspheres, with their uniform diameter and predictable shape, allow for more accurate delivery of therapeutic agents. However, the neovascularization and acidification induced by permanent embolization can potentially lead to tumor invasion and metastasis, impacting the therapeutic effectiveness [13]. To circumvent the prolonged chronic inflammation caused by embolic agents and to facilitate potential repeat treatments, the strategy of using degradable embolization agents is preferred [14]. The integration of biodegradable materials into TACE aims to overcome the challenges posed by permanent embolization. Biodegradable microspheres offer several advantages, including reduced risk of chronic inflammation, the potential to achieve more precise drug release, and the ability to degrade over time, allowing the restoration of normal blood flow after therapeutic action. This approach minimizes ischemia-induced angiogenesis and post-embolization syndrome, improving patient outcomes and reducing long-term side effects. Recent advancements have introduced novel biodegradable embolic materials with promising applications in TACE. For instance, Wang et al. reported a temperature-sensitive hydrogel as a novel degradable embolization material for blood vessels, yet its drug-loading efficacy was not explored [15]. Zeng et al. discussed radiopaque alginate microspheres for transcatheter arterial embolization, and Bai et al. introduced Chitosan Derivative Microparticles, but neither study investigated the anti-cancer effects in animal models [16].

Recently, microalgae demonstrate immense potential as novel biomedical materials. Microalgae have some clear advantages including rapid growth, low cultivation costs, and excellent biocompatibility [17]. They have been extensively utilized including in applications like antimicrobial activity [18], antioxidation [19], bioimaging and drug delivery [20]. For instance, Nannochloropsis is rich in eicosapentaenoic acid, a polyunsaturated fatty acid that is particularly beneficial for cardiovascular health [21]. Haematococcus pluvialis is rich in natural astaxanthin [22], an antioxidant proven to neutralize free radicals and reduce oxidative stress in clinical trials [23]. *Spirulina platensis* (SP) contains compounds such as phycocyanin that exhibit anti-tumor properties [24], capable of inhibiting cancer cell growth and inducing apoptosis [25]. It possesses a strong electronegative charge that enables the binding of positively charged drugs through electrostatic interactions [26]. Compared to other microalgae, the surface of SP has channels which are capable of loading drugs. Its unique spiral structure and strong motility allow it to move to smaller blood vessels achieving embolization. Its micron-sized dimensions (100–500 μm) are similar to those of clinically used embolic microspheres [27], presenting promising potential for clinical application.

Most of the current research on embolic agents for TACE treatment focused on the application of chemically synthesized materials and natural polymer materials [28]. However, there had been no literature reporting the exploration of microalgae as embolic agents. Based on the drug loading capacity, size, morphological and structural characteristics, SP was chosen as the drug carrier to develop a novel embolic agent that addresses the limitations of cTACE by enabling sustained drug release, effective vascular embolization, and enhanced biosafety (Scheme 1). The chemotherapy drug doxorubicin (DOX) was effectively loaded into SP to formulate the drug-microalgae embolic agent (DOX-SP). In vitro studies showed that DOX-SP effectively suppressed the proliferation of liver cancer cells. Furthermore, in vivo experiments demonstrated that DOX-SP could be administered through a catheter into the hepatic artery of rats with HCC tumors. Under the surveillance of a digital subtraction angiography (DSA) X-ray system, DOX-SP effectively obstructed both the primary and secondary vasculature, preventing collateral circulation and reperfusion, as well as inhibiting angiogenesis and ectopic embolization. DOX-SP exhibited pH sensitivity and response to the acidic TME, leading to a controlled release of DOX and facilitating drug accumulation at the tumor site, thereby enhancing its anti-tumor efficacy. Moreover, its biodegradable properties enabled it to completely decompose after completing treatment, avoiding the side effects caused by long-term accumulation. SP represents a potentially groundbreaking, biodegradable TACE material that offers a synergistic approach to combining embolization and chemotherapy in the treatment of hepatocellular carcinoma. This novel natural embolic agent, derived from microalgal biomaterials, holds significant promise for clinical application, presenting a new and promising TACE strategy for the management of liver cancer.

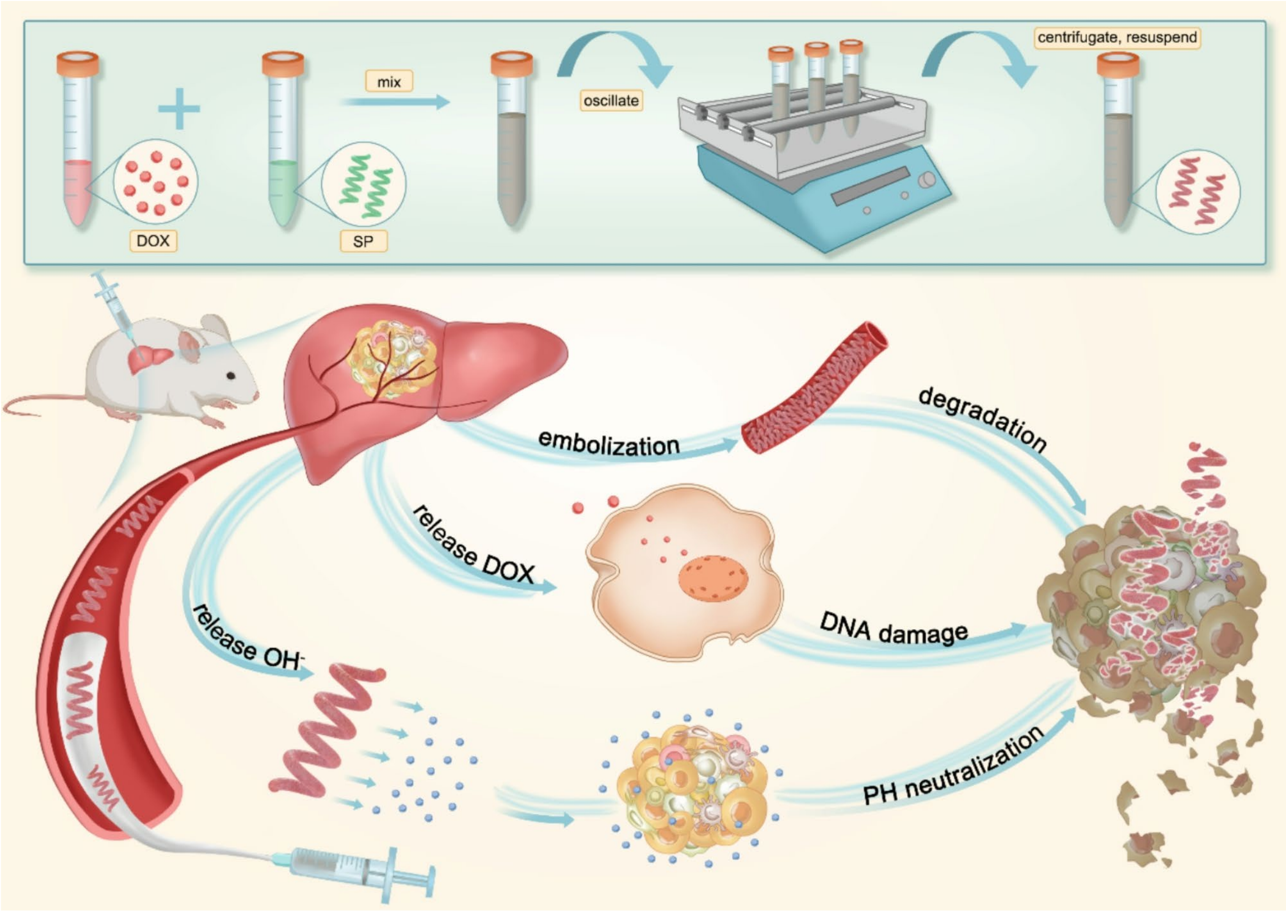

Scheme 1 The DOX loading diagram of SP and the antitumor diagram of DOX-SP against orthotopic HCC. The mixture of SP and DOX was simply shaken to obtain DOX-SP. DOX-SP embolized the tumor-feeding arteries and was capable of slowly releasing DOX to kill tumor cells, while simultaneously improving the acidic environment of the tumor microenvironment

Method

Synthesis, characterization of DOX-SP

SP and DOX were dispersed in ddH_2O, and then oscillated for 12 h in a dark, room-temperature environment. Following this, it was centrifuged at 1000 rpm for 5 min. The supernatant was discarded, and the precipitate was collected for subsequent experiments. The prepared DOX-SP and SP were observed under a fluorescence microscope and a scanning electron microscope (SEM) to examine their morphology and structure. Optical spectra were acquired using a UV – vis – NIR spectrometer (Shimadzu UV-2600, Japan) [29]. Fluorescence emission spectra were measured using a fluorescence spectrophotometer (Shimadzu RF-6000, Japan). Zeta potentials were recorded by a dynamic light scattering system (Malvern Panalytical Zetasizer Nano ZS90, UK).

In vitro anticancer evaluation

Cell proliferation was assessed using the CCK-8 kit to evaluate the cytotoxicity of SP, free DOX and DOX-SP, following the manufacturer's instructions. N1S1 and McA-RH7777 cells were seeded in 96-well plates at a density of 5×10^4 cells/mL in a volume of 100 μL per well and allowed to adhere overnight. The cells were then treated with 100 μL of the respective culture medium containing varying concentrations of SP (3.13, 6.25, 12.5, 25, 50, and 100 μg/mL), DOX (2.5, 5, 10, 20, 40, and 80 μg/mL), and corresponding concentrations of DOX-SP. After a 24-hour incubation period, the complete medium was gently removed, and the cells were washed twice with PBS. The cells were then incubated with 90 μL of serum-free medium and 10 μL of CCK-8 solution for 1 h to evaluate cell viability. The absorbance at 450 nm was measured using the Spark® Multimode Microplate Reader (Tecan, Switzerland).

McA-RH7777 cells were seeded in 12-well plates at a density of 1×10^6 cells/well and incubated overnight. They were then treated with SP (100 μg/mL), DOX (80 μg/mL), and corresponding concentrations of DOX-SP. After a 24-hour incubation period, the complete medium was gently removed, and the cells were stained using the Calcein-AM/PI double stain kit and observed under a fluorescence microscope. The effects of SP, free DOX and DOX-SP on the apoptosis of N1S1 cells were studied using flow cytometry. N1S1 cells seeded in 12-well plates were treated with SP (100 μg/mL), DOX (80 μg/mL) and corresponding concentrations of DOX-SP, and incubated at 37 °C for 24 h. The cells were then collected by centrifugation (300×g, 5 min) and stained using the Annexin V-FITC/PI Apoptosis Detection Kit for flow cytometry analysis [30]. The study was conducted in triplicate.

Arterial cannulation

All animal experiments were conducted in accordance with the protocols approved by the Experimental Animal Center and the Animal Ethics Committee of Zhejiang University. Sprague Dawley (SD) male rats, weighing between 300 and 350 g, were utilized for all animal studies. The experiments on the animals were carried out under general anesthesia with isoflurane gas. The rats were anesthetized, and the hair in the surgical area was shaved and disinfected before performing a laparotomy. A midline incision was made to fully expose the hepatic portal area. Ophthalmic curved tweezers were used to separate the common hepatic artery (CHA) and the gastroduodenal artery (GDA). A 6 – 0 suture was employed to ligate the distal end of the GDA. The proximal end of the GDA and the CHA were sequentially lifted to ensure that the freed segment of the GDA was filled with blood. The PE-10 (RWD) polyethylene catheter was retrogradely inserted into the left hepatic artery (LHA) or the proper hepatic artery (PHA) along the proximal end of the GDA. Various drugs were administered through the catheter at an approximate rate of 0.1 mL/min. After the infusion, the catheter was flushed with 0.1 mL of saline, then carefully withdrawn from the arterial incision, and the GDA was permanently ligated above the insertion site. The abdominal cavity was closed in two layers with 3 – 0 silk thread. Throughout the entire procedure, strict aseptic techniques were meticulously adhered to.

Biodistribution and degradation

1 mg of SP was injected into the PHA, followed by fluorescent imaging of the main organs in vitro at 1 h, 7 days, 14 days, and 28 days post-surgery using the PhotonIMAGER OPTIMA (Biospace, France) (Excitation: 605 nm, Emission: 615–665 nm). Select liver specimens were subjected to hematoxylin and eosin (H&E) staining. Additionally, some tissue samples were prepared for Transmission Electron Microscopy (TEM). These TEM sample sections were examined using an H-7650 TEM (Hitachi, Ibaraki, Japan) at 80 kV of accelerating voltage.

Arterial embolism

0.5 mg of SP was injected into the LHA under laparotomy and the catheter was retracted to the PHA after embolization. 1 mL of trypan blue dye was injected, the rat was sacrificed by decapitation, and the liver was extracted for observation and prepared into frozen sections. The nuclei of the cells were stained with 4-6-diamidino-2-phenylindole (DAPI) for observation under a fluorescence microscope. TAE of the hepatic artery was performed under digital subtraction angiography (DSA). After anesthesia with 1% sodium pentobarbital, the rat was placed in a supine position, and a gentle dissection of the right inguinal region was conducted to isolate the right femoral artery. This procedure was carried out by an experienced senior interventional radiologist. Hepatic arteriography was performed through a 1.5-F microcatheter under continuous X-ray fluoroscopy guidance. The catheter was inserted into the PHA, and a contrast agent was injected for DSA. After embolization with 1 mg and 2 mg of SP in different rats, the microcatheter was removed, the right femoral artery was ligated and the rat was allowed to recover.

The establishment of the HCC model in rats

To establish an in situ HCC model in rats, a cell suspension containing 5×10^6 N1S1 cells mixed with 50 µL of PBS and 50 µL of Matrigel was injected into the left lateral lobe of each rat's liver. Subsequently, the injection site was pressed with a cotton swab for 5 minutes, and the abdominal cavity was closed in two layers with 3 – 0 silk thread. Tumor size was evaluated using magnetic resonance imaging (MRI) (Bruker Biospec 7T) with T2-weighted imaging (T2WI) for confirmation. The acquisition parameters of the sequence were as follows: T2WI, TR/TE = 5000/38 ms, field of view 60 mm × 60 mm, slice thickness 1 mm in the transverse plane, matrix 256 × 256. The tumor volume was calculated using the formula: $V = a * b^2 / 2$ (where 'a' is the long diameter and 'b' is the short diameter perpendicular to 'a').

Pharmacokinetics of DOX

Six HCC rats were randomly divided into two groups: the DOX-SP group and the DOX-LPD group, with a DOX dosage of 1 mg/kg and a LPD dosage of 100 µL per rat. DOX-SP or DOX-LPD was administered through a catheter into the LHA. At different time points post-operation (1, 24, and 48 h), 1 mL of blood was collected from the rat's tail vein into heparinized centrifuge tubes and immediately centrifuged (3000 rpm, 15 min) to collect the plasma. Daunorubicin was added as an internal standard to the plasma samples, which were then analyzed for DOX concentration using liquid chromatography-tandem mass spectrometry (LC-MS) with an API 4000 triple quadrupole instrument (Applied Biosystems, Concord, Ontario, Canada). The retention of DOX in the liver and the distribution in other organs were evaluated through ex vivo fluorescence images (Excitation: 480 nm, Emission: 500–560 nm). HCC samples were prepared as frozen slices, cut into 10 µm thick sections, with cell nuclei stained by DAPI, and observed with Zeiss LSM 880 confocal microscope. DOX fluorescence intensity was semi-quantitatively analyzed using ImageJ software.

Measurement of pH values in vivo and in vitro

SP was suspended in PBS containing 10% FBS at pH levels of 5, 6, and 7, and then incubated at 37 °C on a shaker set at 100 rpm for 24 h. The pH of the solution was measured at 2, 4, 6, 8, 12, and 24 h. The pH-sensitive fluorescent probe BCECF was utilized to detect the pH values of HCC before surgery and 24 h after TAE surgery (1 mg SP). Rats were sacrificed 30 min after intratumoral injection of BCECF, tumor tissues were immediately collected, and fluorescence images were captured with an excitation wavelength of 488 nm and an emission of 522 nm.

In vivo antitumor efficacy

When the in situ N1S1 HCC tumors in rats reached a volume of 400 mm [3], they were randomly divided into five groups ($n = 3$): control, LPD, DOX -LPD, SP and DOX-SP. The dosage of DOX administered to each rat was 1 mg/kg, LPD was 100 µL, and SP was 0.5 mg. The control group was observed without treatment, while the other four groups received different drugs via a catheter placed in the LHA. On days 7 and 14, MRI scans were performed on all rats in each group to measure tumor size. The rats were weighed every other day, and their weights were compared with their initial weights on day 0. On day 14 post-embolization, blood was drawn from the tail vein of rats in each group, and after sedimentation and centrifugation, serum was collected and analyzed for relevant biochemical markers, including alanine aminotransferase (ALT), aspartate aminotransferase (AST), total bilirubin (TBIL), and creatinine (CREA). The collected tumor and major organs were fixed in 4% paraformaldehyde solution, embedded in paraffin, and cut into 5 µm thick sections. These sections were processed for H&E staining and immunohistochemistry (IHC) assays to investigate the expression of Ki67 and CD31. Apoptotic cells were identified using terminal deoxynucleotidyl transferase-mediated dUTP nick end labeling (TUNEL) staining. Histological sections were observed using an optical microscope (Olympus, Tokyo, Japan).

Results and discussion

Characterization of SP and DOX-SP

The SP used as a drug carrier in this study possessed a green color, a spiral shape, a length ranging from 100 to 500 µm, and a surface structure characterized by wrinkles. Due to its high chlorophyll content, SP exhibited a stable red fluorescence when excited at 560 nm (Fig. 1A). The synthesis of DOX-SP was achieved through a straightforward one-step process, involving the continuous stirring of SP and DOX solution overnight. The resulting DOX-SP displayed a red color, indicating a successful combination of red DOX with SP. Furthermore, the DOX-loaded SP retained its ability to emit stable red fluorescence, with no significant alteration in its helical morphology. After loading DOX, scanning electron microscopy (SEM) analysis revealed an increase in the surface roughness of SP (Figure S1), Furthermore,

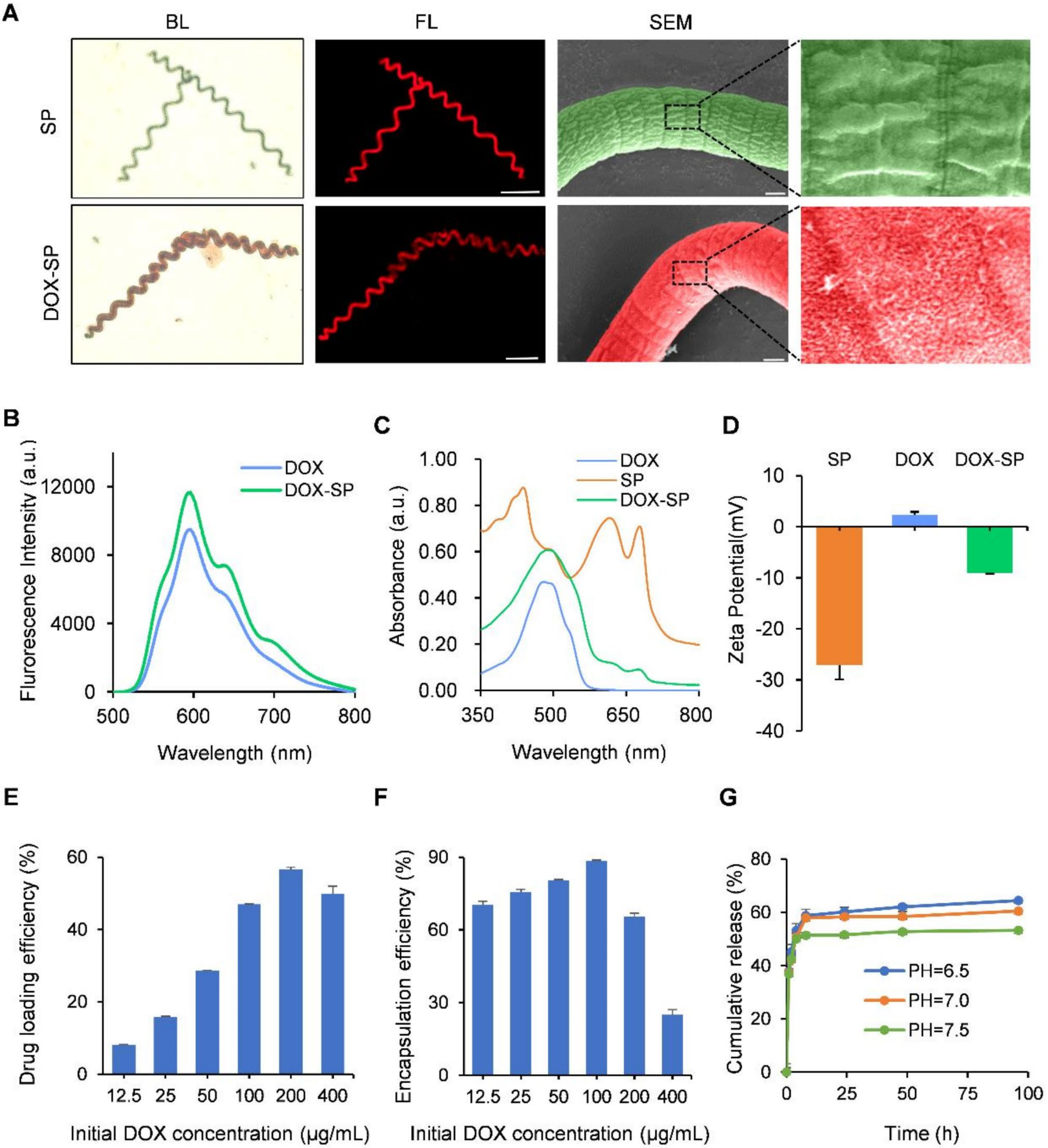

Fig. 1 Characterization of DOX-SP. (**A**) Bright-field (left) and fluorescence (middle) images of SP and DOX-SP, respectively. Scale Bar = 100 μm. High-resolution SEM (pseudo-color) images (right) and magnified images of SP and DOX-SP, respectively. Scale Bar = 2 μm. (**B**) Fluorescence emission spectra of DOX and DOX-SP, respectively. (**C**) UV–vis spectra of SP, DOX and DOX-SP, respectively. (**D**) Zeta potential showed the changes following the loading of SP with DOX (*n* = 3). Data are presented as means ± SD. Drug loading (**E**) and encapsulation efficiency (**F**) of 1 mg SP in different loading concentrations (*n* = 3). Data are presented as means ± SD. (**G**) Cumulative released percentage of DOX over time from DOX-SP in 10% FBS buffer solutions with different pH, respectively

two-photon microscopy images of DOX and SP overlapped well (Figure S2), suggesting the adsorption of DOX onto the SP surface. Subsequent fluorescence spectra (Fig. 1B and S3) and UV-Vis (Fig. 1C) analyses confirmed the successful formation of DOX-SP. The fluorescence characteristics of DOX-SP remained consistent with SP while exhibiting unique UV absorption peaks characteristic of both DOX and SP. The alteration in zeta potential elucidated the mechanism of drug loading, with the zeta potential of SP shifting from – 27.07mV to -9.11mV post-loading, indicating the electrostatic interaction of negatively charged SP with the positively charged DOX (Fig. 1D).

To examine the drug-loading capacity of SP, various concentrations of DOX were introduced to SP suspension. The concentrations of DOX showed a good linear relationship with the OD_{480} values (Figure S4). Within a specific range of DOX concentrations, both drug loading efficiency (DLE) and encapsulation efficiency (EE) exhibited an increase as the concentration of DOX increased. At a DOX concentration of 50 μg/mL, DLE was measured at 28.65 ± 0.12% (Fig. 1E), while EE reached a high of 80.32 ± 0.48% (Fig. 1F), indicating that 1 mg of SP had the capability to carry approximately 0.8 mg of DOX. Subsequently, an investigation into the drug release kinetics of DOX-SP in varying pH environments was conducted to determine the efficacy of drug release from the system. The drug release study involved assessing the cumulative release of DOX at various time intervals in PBS solutions with differing pH levels (Fig. 1G). The findings indicated that at a pH of 7.5, the release curve of DOX reached a plateau after 48 h, with a release rate of 52.71 ± 0.74%. Furthermore, the release of the drug was found to be higher at pH levels of 6.5 and 7 compared to pH 7.5, suggesting that DOX-SP exhibited pH-responsive drug release, with greater release occurring at lower pH levels. This increased release of DOX from DOX-SP in acidic conditions was likely attributed to the proton exchange of the positively charged DOX, leading to enhanced hydrophilicity. Given the acidic nature of TME, this acid-responsive drug release property of DOX-SP might maximize cytotoxic effects on tumors while reducing the adverse effects of the drug on normal tissues.

Cytotoxicity of DOX-SP

In order to evaluate the cytotoxicity of DOX-SP in vitro, various concentrations of SP, free DOX, and DOX-SP were incubated with McA-RH7777 and N1S1 cells for a duration of 24 h and the cell viabilities were assessed using CCK8 assay (Fig. 2A). Cells co-cultured with SP exhibited a higher rate of cell survival, whereas those co-cultured with DOX and DOX-SP demonstrated a lower rate of cell survival, with the survival rate decreasing progressively with increasing DOX concentration. At a concentration of 100 μg/mL of SP, the survival rate of McA-RH7777 cells was measured at 64.12 ± 10.03%, and that of N1S1 cells was 72.24 ± 5.06%, indicating favorable biocompatibility of SP. At a DOX concentration of 80 μg/mL, the cell viability of McA-RH7777 cells treated with free DOX was determined to be only 3.15 ± 0.74%, while those treated with DOX-SP exhibited a viability of only 16.03 ± 1.43%. Similarly, N1S1 cells treated with free DOX and DOX-SP showed viabilities of 6.95 ± 0.31% and 7.97 ± 0.50%, respectively, with no statistically significant difference between the two groups. These findings provided evidence of the significant anti-tumor efficacy of DOX-SP, which was comparable to that of free DOX.

To further confirm the anti-tumor efficacy of DOX-SP, we assessed its ability to induce apoptosis in N1S1 cells (Fig. 2B and C). Analysis of FITC-Annexin V/PI-stained cells by flow cytometry revealed that a concentration of 100 μg/mL of SP resulted in only 34.01 ± 0.63% apoptosis. Conversely, at a concentration of 80 μg/mL of DOX, the apoptosis rate of N1S1 cells induced by DOX-SP reached 96.69 ± 0.79%, which was comparable to that of free DOX, suggesting that DOX-SP exhibited similar anti-tumor effects as DOX. The cytotoxicity of various drugs on McA-RH7777 cells was assessed using Calcein-AM/PI double staining (Fig. 2D). Both the free DOX group and the DOX-SP group caused a large number of dead cells (red fluorescence), and no significant living cells were observed (green fluorescence). The results of flow cytometry and live/dead cell staining showed a consistent trend with the results of CCK8, confirming the in vitro anti-tumor ability of DOX-SP against hepatocellular carcinoma.

The biodistribution and degradation of SP

SP was suspended in PBS containing 10% FBS and then incubated for 7, 14, and 28 days (Fig. 3A). Morphological observations using microscopy and SEM revealed that SP exhibited a complete spiral shape at the beginning (Fig. 3B). By day 7, compared to its initial state, the spiral structure of SP began to fragment, shortening to approximately 50 μm in length. By day 14, it transformed into cylindrical shapes approximately 5–20 μm in length and SP could still be excited to emit red fluorescence (Figure S5). By day 28, the spiral structure was further fragmented and reduced in size, with lengths ranging between 1 and 10 μm, and the fluorescence could no longer be detected. Overall, these observations indicated a gradual fragmentation and size reduction of SP over time, demonstrating its biodegradability.

Fluorescence images enabled us to discern the distribution of SP within the liver following its injection into the hepatic artery (Fig. 3C). SP signals were not observed in other major organs, indicating the absence of ectopic embolization. Over time, the SP within the liver

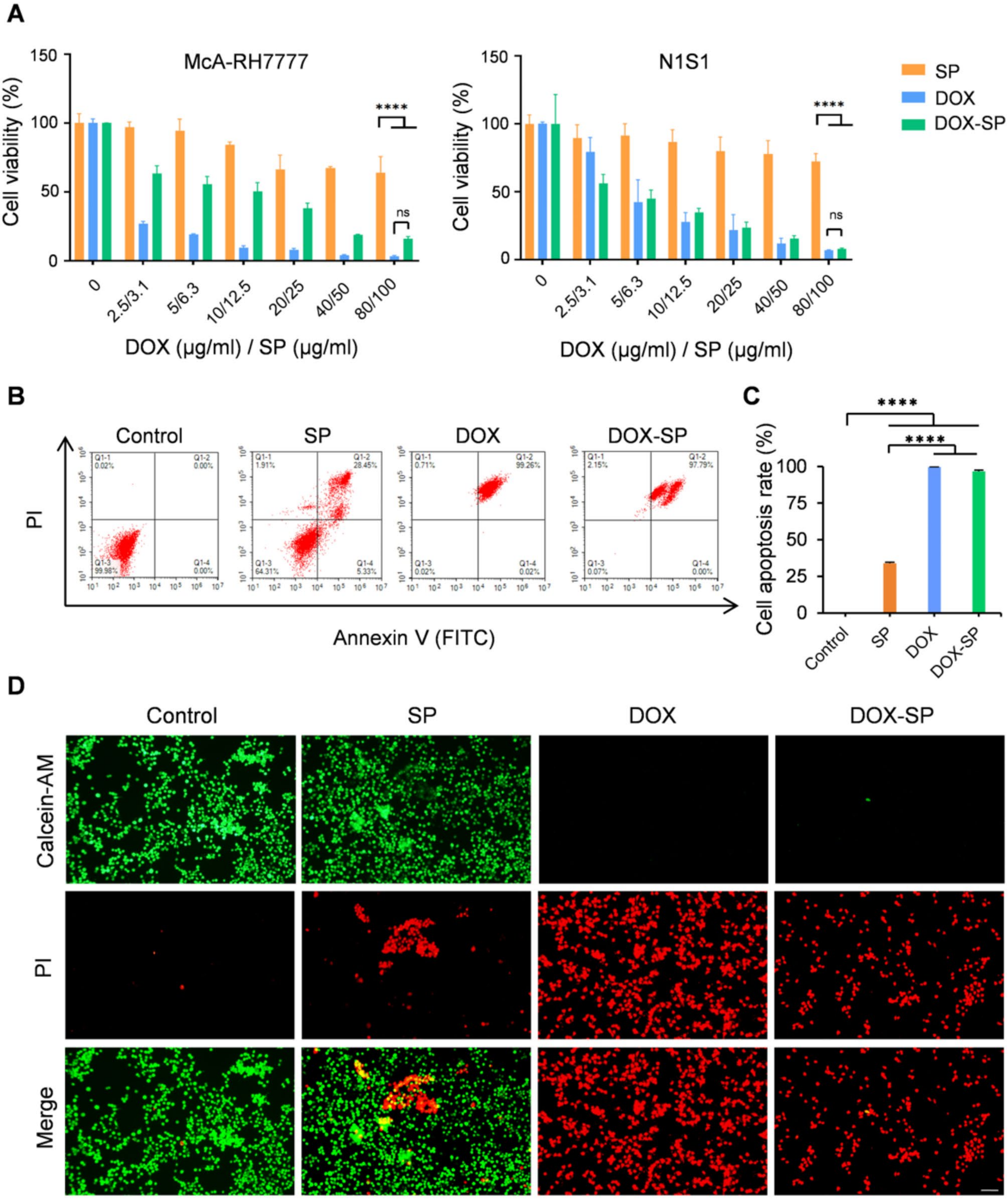

Fig. 2 The antitumor efficacy of DOX-SP in vitro. (**A**) Cell viability of N1S1 cells and McA-RH7777 cells after incubation with series concentrations of SP, DOX and DOX-SP for 24 h. (**B**) Flow cytometry results of N1S1 cells apoptosis after different treatments for 24 h. (**C**) Quantification of cell apoptosis rate in (**B**). Data are presented as means ± SD. (**D**) Fluorescence microscopic images of McA-RH7777 cells costained with calcein AM (green, live cells) and propidium iodide (red, dead cells) after being incubated with SP, DOX and DOX-SP for 24 h. Scale bars = 100 μm. A and C were analyzed for group differences using a one-way ANOVA, with a *p*-value < 0.05 indicating significant differences

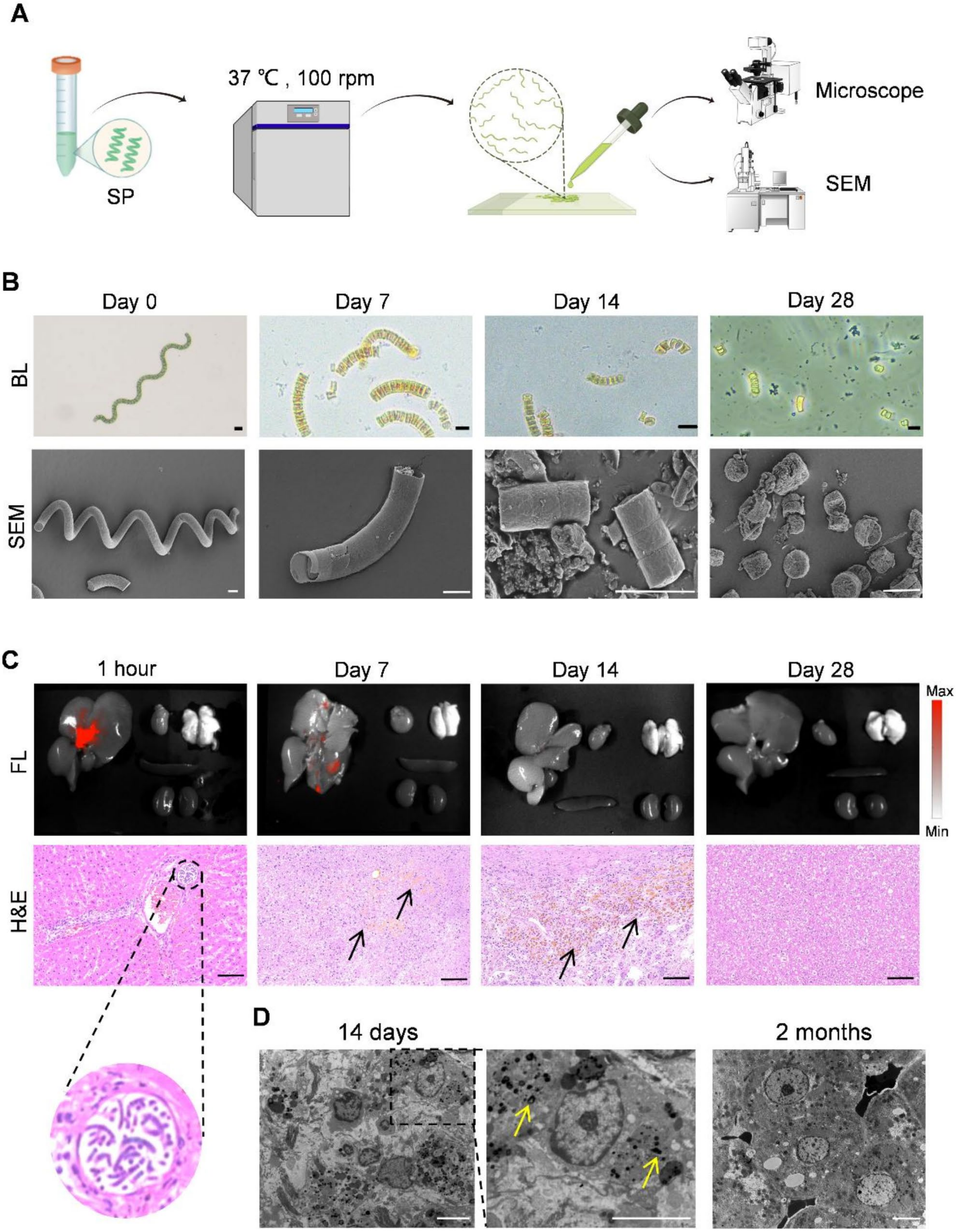

Fig. 3 (See legend on next page.)

(See figure on previous page.)

Fig. 3 The biodistribution and degradation of SP. (**A**) The schematic diagram of SP degradation in vitro. (**B**) Bright-field (Scale Bar = 10 μm) and SEM (Scale Bar = 5 μm) images of DOX-SP after degradation in vitro for 0, 7, 14 and 28 days, respectively. (**C**) Fluorescence images and relative liver tissue H&E staining of DOX-SP after embolization in vivo for 1 h, 7 days, 14 days and 28 days, respectively. Yellow degradation products of SP were observed in the liver (black arrow). Scale Bar = 100 μm. (**D**) TEM images of the liver tissue after degradation in vivo for 14 days (left) and 2 months (right) following embolization. Degradation products of SP were observed in the liver cell (yellow arrow). Scale Bar = 5 μm

underwent degradation, leading to a diminution of the fluorescence signal. Liver pathological sections clearly revealed that the SP had completely filled the arteries post-intervention for 1 h. Yellow degradation products of SP were detected within the liver on the 7th and 14th days, while no significant residues were evident in the liver on the 28th day. TEM images at 14 days showed hepatic phagocytic clearance of SP fragments (Fig. 3D), and by two months post-intervention, no significant SP residues were observed within hepatocytes. However, thrombosis was evident in the hepatic sinusoids, suggesting that SP embolization could facilitate thrombus formation, thereby preventing vascular recanalization. We hypothesized that the degradation period of SP ranges from 4 to 8 weeks. Biodegradable microspheres have become a focal point in embolic agent development. The embolization duration varies with different biodegradable materials. For instance, starch microspheres can provide vascular occlusion for up to 80 min [31], while the degradation time of gelatin microspheres was related to their crosslinking degree and particle sizes [32]. In our study, we found that SP showed a 90% reduction in average diameter within two weeks of in vitro degradation, and became pathologically undetectable in vivo within 4–8 weeks, demonstrating good safety and tolerability.

In vivo embolization effect of SP

To further validate the embolization effect of SP, DSA was employed to observe hepatic blood flow (Fig. 4A). DSA imaging showcased the distribution of hepatic arterial vessels prior to embolization (Fig. 4B). Following the injection of 1 mg SP into the PHA, X-rays failed to detect the contrast agent within the terminal hepatic arteries. However, after administering 2 mg SP, the mainstream vessels were adequately embolized, confirming successful arterial embolization.

Following the injection of 0.5 mg SP into the LHA, the catheter was retracted to the PHA and then blue ink was injected (Fig. 4C). It was observed that the ink failed to stain the liver lobes supplied by the LHA, whereas the lobes supplied by the right hepatic artery were deeply stained in blue (Fig. 4D). In the frozen sections of the left liver lobes, SP emitting red fluorescence was seen intertwined upon excitation at a wavelength of 560 nm, filling blood vessels of various diameters. This indicated that SP was capable of embolizing arteries of different diameters. SP clusters were visible under the bright field (Fig. 4E) and fluorescence field (Fig. 4F) of the microscope. These results highlighted SP's excellent flow properties and embolization characteristics, achieving complete occlusion at all arterial levels, thereby preventing collateral circulation. The resultant ischemia or hypoxia-induced degeneration and necrosis in the tumor, thereby yielding superior therapeutic outcomes. The common embolic materials were spherical in shape. Nevertheless, many researchers are exploring embolic materials beyond spherical particles to achieve better embolization effects. Cai and colleagues recently reported that bullet-shaped microparticles might exhibit superior embolic performance compared to spherical ones [33]. Luo et al. developed shape-anisotropic microembolics for transarterial embolization treatment [34]. In our study, we observed that SP appeared a helical shape, intertwining and accommodating blood vessels of various diameters. Utilizing DSA-guided TAE, we tested the in vivo feasibility of intra-arterial infusion of SP. Small doses of SP were capable of occluding peripheral vessels, while larger doses could obstruct major arteries such as the LHA, with no ectopic embolization observed. This suggests a significant potential for SP as vascular embolic material.

Release of DOX and the impact of SP on pH

The pharmacokinetic behavior of chemotherapy drugs plays a pivotal role in their antitumor efficacy and biosafety. Exploring the distribution of DOX at various time points within tumors and blood was essential. Both the DOX-SP and DOX-LPD groups displayed DOX fluorescence signals near the hepatic portal area 1 h post-embolization (Fig. 5A). Notably, the DOX signal near the tumor was still discernible at 24 and 48 h post-surgery in the DOX-SP group, whereas in the DOX-LPD group, the signal was exceedingly faint and virtually undetectable at these time intervals. Compared with DOX-LPD group, the fluorescence of DOX was more significant in the DOX-SP group 24 h post-embolization (Fig. 5B). In vital organs such as the heart, spleen, lungs, and kidneys, no significant signals were observed in either group. Confocal microscopy assessment of tumor frozen sections revealed the presence of DOX signals (red) within tumor cells following DAPI staining (blue), indicating successful delivery of chemotherapy drugs in both groups (Fig. 5C). The intensities of both groups were comparable after 1 h post-operation. However, the DOX-SP group maintained a higher fluorescence intensity than the DOX-LPD group after 24 and 48 h postoperatively (Fig. 5D). Fluorescence quantification at 24 h post-surgery demonstrated a

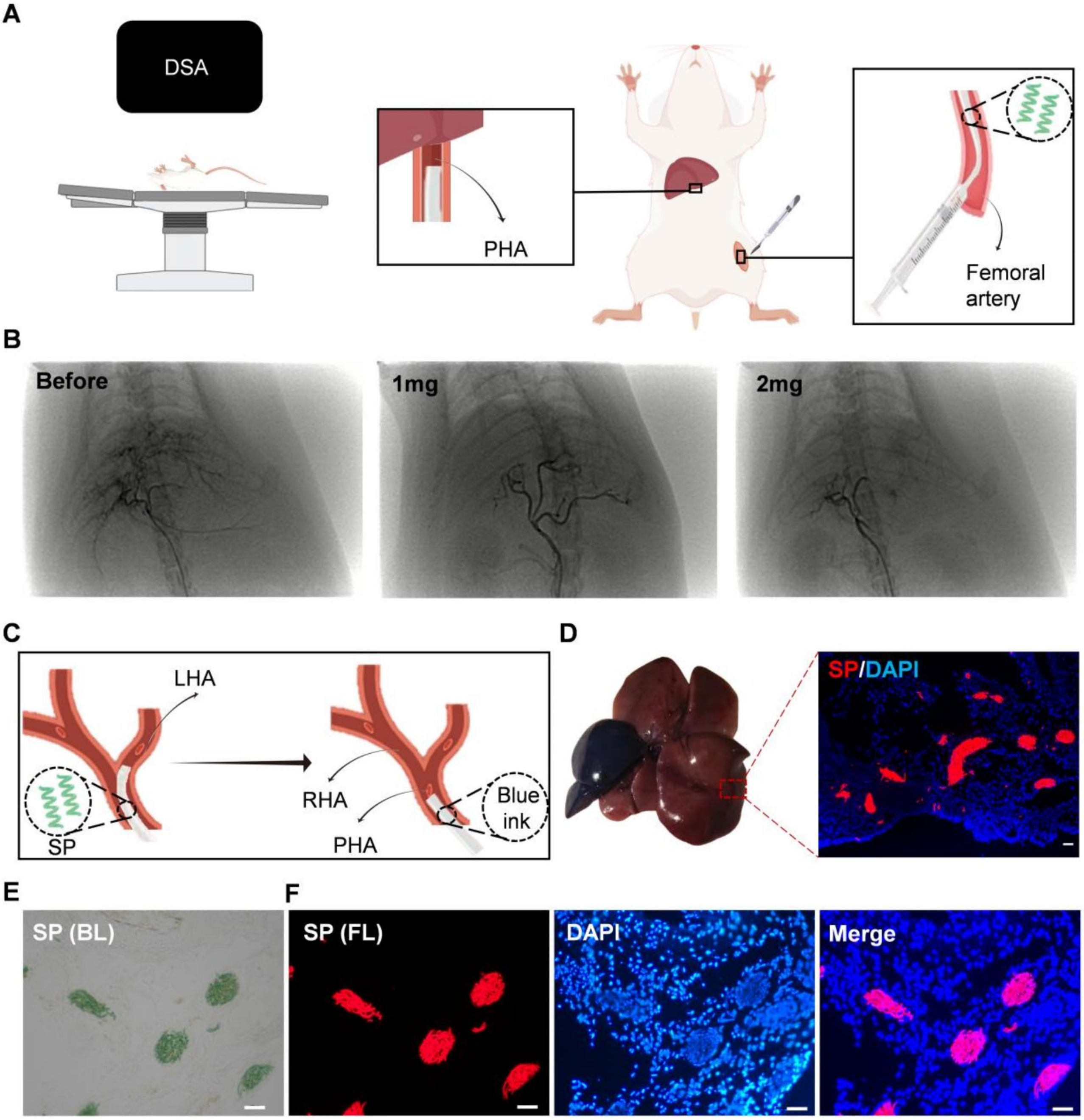

Fig. 4 The embolization effect of SP in vivo. (**A**) The schematic diagram of the rats undergoing DSA. (**B**) DSA images of pre-intervention (left) and post-intervention (middle and right) with different amounts of SP. (**C**) The schematic diagram of liver staining with blue ink in rats after embolization. (**D**) Left, staining of the liver after embolization of the LHA with SP and the lobes supplied by the right hepatic artery were deeply stained in blue. Right, fluorescence image of SP in the blood vessels. (**E**) Frozen sections images of the rat's normal liver for 1 h after SP (green) embolization. Scale Bar = 100 μm. (**F**) Fluorescence image of SP in the blood vessels of the liver (red indicates SP; blue indicates the cell nucleus). Scale Bar = 100 μm

significant difference ($p < 0.05$) between the two groups. Employing the LC-MS method, the standard curve of DOX in plasma was successfully established (Figure S6). The retention time of DOX was approximately 3.2 min, and the retention time of daunorubicin was approximately 3.6 min (Figure S7). The DOX concentrations were assessed in plasma at different postoperative intervals, thereby obtaining a plasma drug concentration-time curve (Fig. 5E). A comparative analysis of the plasma concentration curves between the DOX-SP and DOX-LPD groups revealed that the DOX concentration in the DOX-LPD group reached 247.35 ± 123.69 ng/mL one-hour post-embolization, compared to 75.78 ± 26.51 ng/mL in the DOX-SP group. The plasma DOX

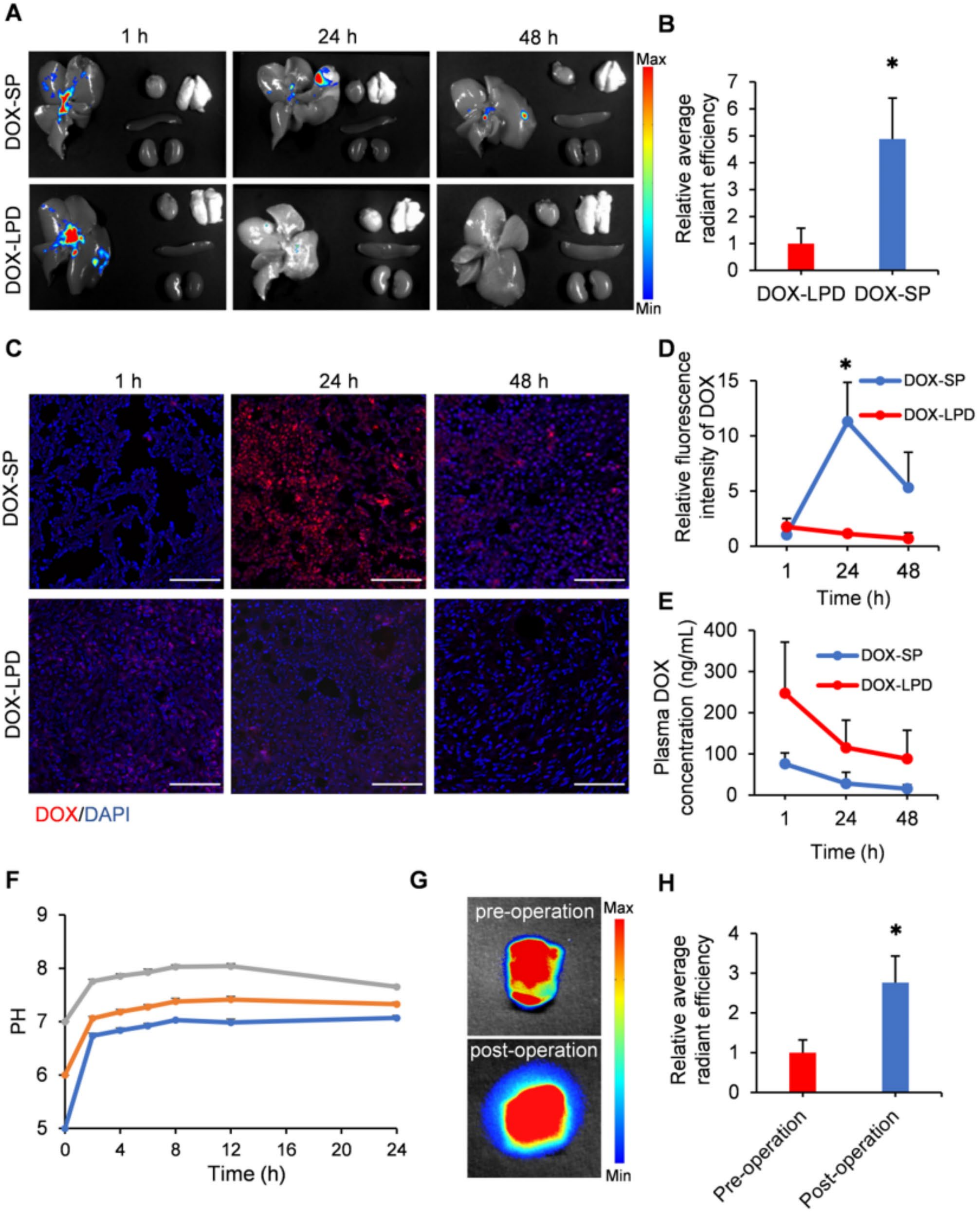

Fig. 5 (See legend on next page.)

(See figure on previous page.)

Fig. 5 Release of DOX and the impact of SP on pH. (**A**) Fluorescence imaging of DOX in the liver at different time points in the DOX-SP group and DOX-LPD group, respectively. (**B**) Quantitative analysis of the fluorescence signals of DOX in the tumor after 24 h. ($n = 3$). Data are presented as means ± SD. (**C**) Fluorescence images of the frozen sections were obtained after TACE in experiment a, respectively. Red fluorescence represents the DOX, and blue means the live cancer cell nucleus with DAPI staining. Scale bars, 100 µm. (**D**) Fluorescence quantification of DOX in (**C**) ($n = 3$). Data are presented as means ± SD. (**E**) The concentration of DOX in the peripheral blood of N1S1 tumor model rats treated with DOX-SP-TACE and DOX-LPD-TACE for 1, 24 and 48 h. ($n = 3$). Data are presented as means ± SD. (**F**) The changes of pH over time in buffer solutions with different initial pHs containing SP ($n = 3$). Data are presented as means ± SD. (**G**) Preoperative and postoperative fluorescence images of the tumor stained with BCECF AM. (**H**) Fluorescence quantification of (**G**) in two groups ($n = 3$). Data are presented as means ± SD. B, D, and H were analyzed for group differences using a t-test, with a p-value < 0.05 indicating significant differences

concentrations in both groups decreased over time, and at each time point, the concentration was lower than that in the DOX-LPD group.

The in vivo distribution results further indicated that the DOX fluorescence signals in the DOX-SP group were concentrated in the tumor with the normal liver exhibiting relatively lower DOX levels. This suggests that the drug was localized to the tumor without dispersing to other vital organs. The DOX-SP group exhibited superior localized slow-release effects and lower peripheral drug concentrations, resulting in reduced systemic toxicity compared to the DOX-LPD group. This implies that DOX loaded on SP may possess slow drug release characteristics and a more effective antitumor impact. Accumulating drugs at high concentrations within the tumor represents a crucial strategy for enhancing the efficacy of HCC treatments. Liu et al. discovered that polymersome-stabilized DOX-LPD emulsions can prolong liver retention of DOX for highly efficacious chemoembolization therapy [35]. Nanomaterials [36] had also attracted attention in the treatment of liver cancer [37]. Li et al. employed DOX-loaded hollow gold nanospheres for the delivery of DOX to HCC [38]. In our study, we discovered that DOX-SP achieved stable and sustained delivery of DOX to tumor tissues, reducing plasma drug concentration. This approach minimizes the adverse effects of the rapid entry of anticancer drugs into the systemic circulation, thereby achieving a more effective anticancer outcome.

Due to the TME changes post-embolization, such as hypoxia and decreased pH, leading to suboptimal therapeutic outcomes. To investigate the effect of SP on pH levels both in vivo and in vitro, we placed SP in PBS containing 10% FBS at different pH levels for observation. The study results indicated that the pH values in all three groups rose rapidly within 2 h. After 24 h, the pH values of the three groups tended to be neutral (Fig. 5F). It is commonly believed that TACE surgery might induce tumor hypoxia and exacerbate the acidic TME. To explore the impact of SP embolization on the TME, we compared the pH values within the tumor using BCECF AM (Fig. 5G). Compared to preoperative levels, an increase in tumor pH was observed 24 h after SP embolization (Fig. 5H). TAE can induce vascular occlusion, resulting in nutritional deprivation of the tumor. Most cancer cells generate energy through glycolysis, leading to an increase in metabolic by-products such as lactate. The extracellular pH of tumors is lower than that of normal tissues [39]. The pH of the tumor microenvironment (TME) played a significant role in tumor cell metabolism and immune cell function. Tumor cells tended to obtain energy through the glycolytic pathway [40], a process that produced large amounts of lactic acid, resulting in an acidic TME. The acidic extracellular environment was closely associated with increased tumor cell invasiveness, as tumors regulated pH to influence their metastatic potential. Immune cells were highly sensitive to pH fluctuations. The immunosuppressive TME was characterized by low pH, hypoxia, glucose deprivation, and lactate accumulation, which collectively impaired immune responses [41]. T cells, macrophages, and dendritic cells required specific pH conditions to execute their immune surveillance and cytotoxic functions [42]. In an acidic environment, T cell activation and effector functions, such as cytotoxicity, were inhibited, which presented a major barrier to their proper proliferation, differentiation, and function. Elevating the pH in the TME could have potentially restored T cell function, enhancing their ability to recognize and eliminate tumor cells. Moreover, macrophages often adopted a pro-tumoral M2 phenotype in acidic conditions [43]. A more alkaline TME might have facilitated macrophage polarization toward the M1 phenotype, which was associated with stronger anti-tumor activity. By modulating the acidic TME, the metabolic balance of tumor cells could have been disrupted, leading to growth inhibition, while simultaneously alleviating immune suppression. Common biodegradable microspheres included chitosan-cellulose microspheres, polyethylene glycol methacrylate (PEGMA) microspheres, poly (D, L-lactic acid) (PDLA, PLLA), and poly (lactic-co-glycolic acid) (PLGA) microspheres. PLGA, a hydrophobic and biodegradable polymer, hydrolyzes in the body to produce lactic and glycolic acids [44]. The presence of lactate may exacerbate the acidification of the TME, inhibiting the anti-tumor ability of immune cells within the TME [45]. This condition can even drive tumor angiogenesis [46] and facilitate immune evasion [47]. Considering that most TMEs are acidic, numerous studies have focused on modulating this acidic environment to enhance anti-tumor therapy

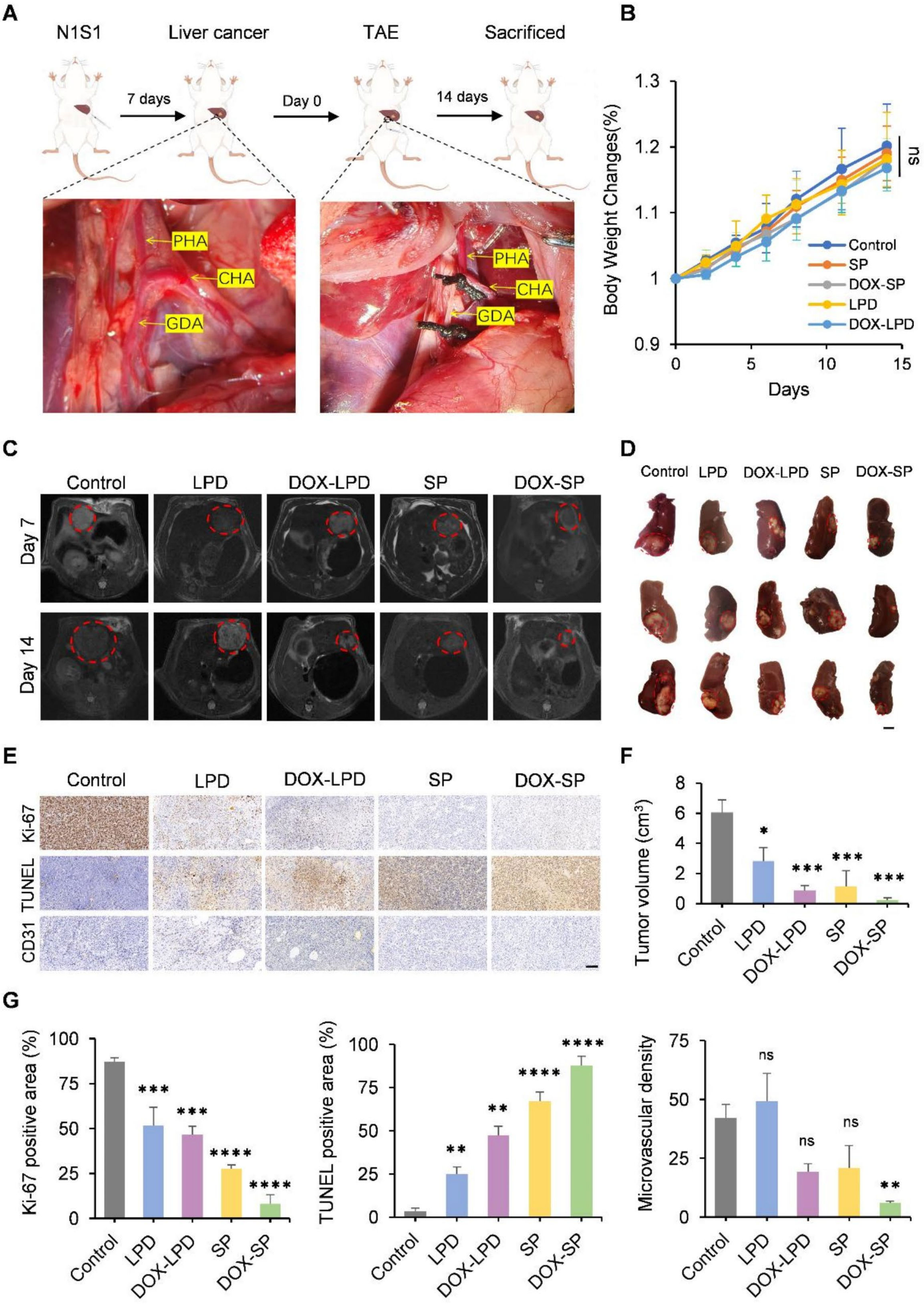

Fig. 6 (See legend on next page.)

(See figure on previous page.)

Fig. 6 The antitumor efficacy of DOX-SP in vivo. (**A**) Schematic diagram of animal experiments. (**B**) Body weight changes of rats after surgery ($n = 3$). Data are presented as means ± SD. (**C**) MRI images of the liver after 7 and 14 days from different groups, respectively. (**D**) Images of the liver after 14 days of treatment in different groups, respectively. Scale Bar = 1 cm. (**E**) Represented immunohistochemical (Ki-67, TUNEL and CD31) images of the HCC after different treatments for 14 days. Scale bar = 100 μm. (**F**) Comparison of tumor volume among groups of (**D**). (**G**) Quantification of Ki-67, TUNEL and microvascular density ($n = 3$). Data are presented as means ± SD. B, F, and G were analyzed for group differences using a one-way ANOVA, with a p-value < 0.05 indicating significant differences

[48]. For instance, Dong et al. encapsulated catalase within calcium carbonate ($CaCO_3$) to neutralize tumor acidity, alleviate hypoxia, and inhibit lactate production [49]. Similarly, Zhang et al. supplied alkaline l-arginine to the tumor to reconstruct the TME, thereby enhancing the anti-tumor immune response [50]. Similarly, Zhang et al. reported that the reaction of $CaCO_3$ with protons neutralizes the pH of HCC, improving cancer treatment through tumor pH neutralization [51]. In our research, we observed that the growth environment of SP is alkaline [52]. In vitro experiments confirmed that SP raises the pH of acidic buffers. SP can not only respond to low pH values for drug release but also significantly increase the pH within the tumor, thus modulating the TME. Phycocyanin (PC) was one of the major degradation products of SP. PC possessed various beneficial properties, including antioxidant, anticancer, anti-inflammatory, hepatoprotective, and immunomodulatory effects [53]. It had been proven to be safe and non-toxic for human health. PC was an oligomeric peptide composed of two polypeptide subunits (α and β), each containing approximately 160–180 amino acid residues [54]. The amino acid residues in its protein structure, such as amino or carboxyl groups, may directly interact with hydrogen ions, thereby contributing to the regulation of local acidic microenvironments by buffering pH levels. Therefore, we speculated that SP could enhance anti-tumor efficacy by improving the TME.

The antitumor efficacy of DOX-SP against orthotopic HCC

N1S1 cells were employed to establish a primary hepatocellular carcinoma model in rats, which received transarterial embolization 7 days post tumor growth. Preoperative and postoperative photographs of the surgical area in rats are presented as shown, with the GDA being permanently ligated (Fig. 6A). To investigate the antitumor efficacy of different drugs, tumor-bearing rats were randomly divided into five groups ($n = 3$): Control, LPD, DOX-LPD, SP, and DOX-SP. No significant differences in body weight were observed among the groups during treatment (Fig. 6B). Tumor growth in each group was monitored via MRI at one and two weeks following embolization (Fig. 6C). Following two weeks of treatment, blood was drawn from the rats' tail veins for blood tests. Upon euthanasia, the liver and other major organs were harvested for observational analysis, with macroscopic photographs of the rats' livers displayed (Fig. 6D). The differences in liver tumor volume growth rates among the groups were statistically significant ($P < 0.05$). The control group exhibited the largest tumor volume (Fig. 6F). The LPD group's liver tumor volume significantly increased compared to the other three groups, indicating that mere LPD perfusion has a lesser therapeutic effect on HCC. The tumor volume in the SP group was second only to the LPD group, suggesting that SP could inhibit tumor growth to a certain extent. The tumors treated with DOX-LPD grew from 400 mm3 to 869.50 ± 338.11 mm [3] over 14 days, whereas those treated with DOX-SP saw a reduction to 31.33 ± 0.84 mm [3] within 14 days post-TACE, significantly lower than the other treatment groups, indicating that DOX-SP more effectively inhibits tumor growth compared to DOX-LPD.

The evaluation of tissue apoptosis, antitumor proliferation efficacy, and angiogenesis was conducted through the observation of TUNEL, Ki-67, and CD-31 IHC staining (Fig. 6E). The control group displayed a high cell proliferation index (87.33 ± 2.05%) and the DOX-SP group exhibited the lowest level of proliferation at 8 ± 5.10% (Fig. 6G). The expression of TUNEL was the exact opposite, with the percentage of DOX-SP positive cells significantly higher than the other groups, demonstrating a significant difference ($P < 0.05$). Additionally, compared to other treatment groups, the expression of CD-31 in tumors treated with DOX-SP was markedly reduced. Thus, DOX-SP exhibited antitumor efficacy by promoting tumor necrosis, inhibiting angiogenesis, and suppressing cell proliferation.

Biocompatibility assessment

Throughout the observation period, there were no fatalities in the rats. H&E staining of the main organs in rats post-TAE surgery with SP on days 7, 14, and 28 revealed no significant tissue damage or inflammatory lesions. No ectopic embolism was detected in major organs such as the heart, spleen, lungs, and kidneys (Fig. 7A). 14 days post-embolization, whole blood was collected from the rats for complete blood count analysis and serum was collected to measure key hematological biochemical markers. The levels of WBC, RBC, HGB, PLT, ALT, AST, Cr, BUN, and TBIL were all within normal ranges (Fig. 7B). In conclusion, the SP used in this study demonstrated commendable biosafety.

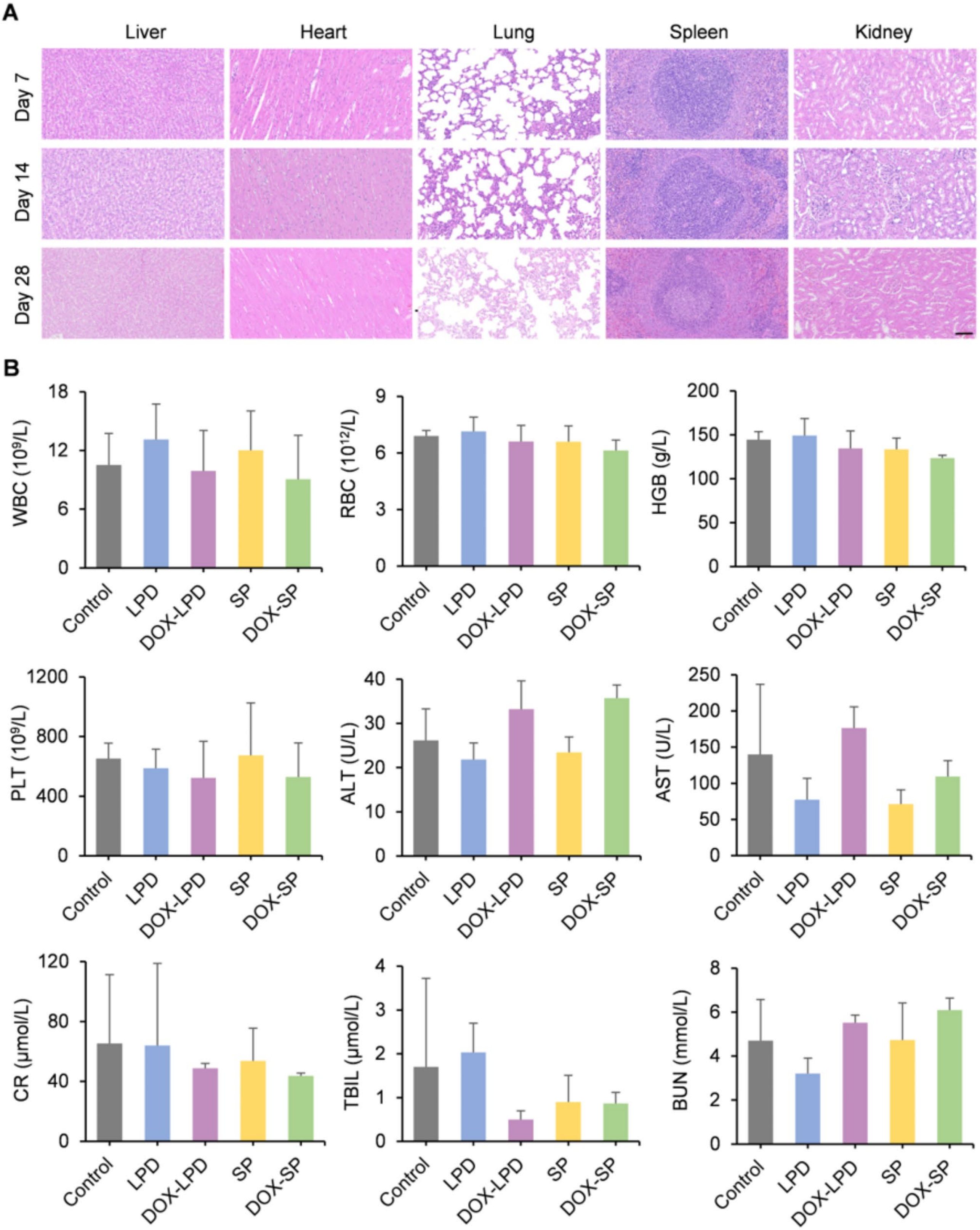

Fig. 7 Long-term safety evaluation. (**A**) Represented HE images of the major organs of the rats after different treatments for 14 days, respectively. Scale bar = 100 μm. (**B**) Hematological tests and serum biochemical tests of the rats of each group after different treatments for 14 days (*n* = 3). Data are presented as means ± SD

Study limitations

This study has certain limitations. Firstly, the decomposition products of SP are not fully clarified, necessitating mid to long-term in vivo implantation to determine the actual degradation rate. Secondly, the rat tumors were generated by directly implanting rat HCC cells into normal liver parenchyma, lacking the typical underlying liver cirrhosis seen in human HCC patients. Additionally, the sample size for each group is relatively small, with only three rats per group, which could diminish the statistical power of the findings.

Conclusion

TACE remains the standard treatment for patients with intermediate-stage HCC. The current clinical efficacy of TACE was not entirely satisfactory. DOX-LPD was unstable, leading to the rapid release of drugs, resulting in a higher concentration of the drug being released into the bloodstream. Inspired by natural microalgae, this study successfully developed an ideal hepatic artery embolizing agent, DOX-SP. The raw materials for DOX-SP are readily obtainable with low costs, and its synthesis process is straightforward, offering the potential for industrialization. DOX-SP possesses the desired attributes of an ideal vascular embolizing agent for TACE: biodegradability, excellent biocompatibility, sensitivity to acidic pH, enhancement of TME pH, and the capability for high-performance embolization and sustained release of the anticancer drug. SP and DOX demonstrated synergistic antitumor effects. This novel material holds promise as a new vascular embolizing agent, offering exceptional therapeutic effects in TACE treatment for HCC. DOX-SP has the potential for clinical translation and practical application, and further exploration of its long-term biosafety for clinical application as an interventional therapeutic alternative is still necessary.

Supplementary Information

The online version contains supplementary material available at https://doi.org/10.1186/s12951-025-03290-5.

Supplementary Material 1

Acknowledgements

We thank Hong Xiaoli from the Core Facilities, Zhejiang University School of Medicine for their technical support.

Author contributions

K.W., D.Z., and L.Y. contributed equally to this work. K.W., D.Z., L.Y., C.Z., and Q.H. performed experiments. K.W., D.Z., and L.Y. completed the data analysis and manuscript writing. M.Z. and Z.T. designed and supervised the project. All authors have given support to the final version of the manuscript.

Funding

This work was supported by the National Key R&D Program of China (2022YFA1105200), the Natural Science and Foundation of Shandong Province (ZR2023ZD30), the Binjiang Institute of Zhejiang University (ZY202205SMKY007), the Medical Science and Technology Project of Zhejiang Province (2022RC024), the Leading Earth Goose Program of Zhejiang Province (2025C02132), and the Leading Innovative and Entrepreneur Team Introduction Program of Zhejiang (2022R01002).

Data availability

No datasets were generated or analysed during the current study.

Declarations

Ethics approval and consent to participate

All experimental involving animals were approved by the Experimental Animal Ethics Committee of the fourth affiliated hospital Zhejiang University School of Medicine.

Conflict of interest

The authors declare no conflict of interest.

Received: 30 November 2024 / Accepted: 3 March 2025

References

1. Bray F, et al. Global cancer statistics 2022: GLOBOCAN estimates of incidence and mortality worldwide for 36 cancers in 185 countries. CA Cancer J Clin. 2024;74:229–63.
2. Llovet JM, et al. Molecular pathogenesis and systemic therapies for hepatocellular carcinoma. Nat Cancer. 2022;3:386–401.
3. Thomas MB, et al. Hepatocellular carcinoma: consensus recommendations of the National Cancer Institute clinical trials planning meeting. JCO. 2010;28:3994–4005.
4. Zhang W, et al. Lenvatinib plus anti-PD-1 antibodies as conversion therapy for patients with unresectable intermediate-advanced hepatocellular carcinoma: a single-arm, phase II trial. J Immunother Cancer. 2023;11:e007366.
5. Xie D, Shi J, Zhou J, Fan J, Gao Q. Clinical practice guidelines and real-life practice in hepatocellular carcinoma: A Chinese perspective. Clin Mol Hepatol. 2023;29:206–16.
6. Llovet JM, et al. Locoregional therapies in the era of molecular and immune treatments for hepatocellular carcinoma. Nat Rev Gastroenterol Hepatol. 2021;18:293–313.
7. Raoul J-L, et al. Updated use of TACE for hepatocellular carcinoma treatment: how and when to use it based on clinical evidence. Cancer Treat Rev. 2019;72:28–36.
8. Lewis AL, Dreher MR. Locoregional drug delivery using image-guided intra-arterial drug eluting bead therapy. J Controlled Release. 2012;161:338–50.
9. Szemitko M, Falkowski A, Modrzejewska M, Golubinska-Szemitko E. Efficacy and safety of liver chemoembolization procedures, combined with FOLFIRI chemotherapy, in First-Line treatment of metastatic colorectal Cancer in patients with oncogene mutations. Cancers (Basel). 2023;16:71.
10. Han T, et al. The clinical safety and efficacy of conventional transcatheter arterial chemoembolization and drug-eluting beads-transcatheter arterial chemoembolization for unresectable hepatocellular carcinoma: A meta-analysis. Biosci Trends. 2019;13:374–81.
11. Grumme J, et al. Transarterial chemoembolization for hepatocellular carcinoma: quality of life, tumour response, safety and survival comparing two types of drug-eluting beads. Abdom Radiol. 2020;45:3326–36.
12. Kwok PC, et al. A randomized clinical trial comparing autologous blood clot and gelfoam in transarterial chemoembolization for inoperable hepatocellular carcinoma. J Hepatol. 2000;32:955–64.
13. Bao MH-R, Wong CC-L, Hypoxia. Metabolic reprogramming, and drug resistance in liver Cancer. Cells. 2021;10:1715.
14. Yuan G, et al. Multifunctional nanoplatforms application in the transcatheter chemoembolization against hepatocellular carcinoma. J Nanobiotechnol. 2023;21:68.
15. Wang Q, et al. Precision embolism: biocompatible Temperature-Sensitive hydrogels as novel embolic materials for both mainstream and peripheral vessels. Adv Funct Mater. 2021;31:2011170.
16. Zeng J, et al. Radiopaque and uniform alginate microspheres loaded with tantalum nanoparticles for real-time imaging during transcatheter arterial embolization. Theranostics. 2018;8:4591–600.

17. Sampath S, et al. A review on algal mediated synthesis of metal and metal oxide nanoparticles and their emerging biomedical potential. J Biotechnol. 2022;360:92–109.
18. Vazquez-Ayala L, et al. Chitosan sponges loaded with Metformin and microalgae as dressing for wound healing: A study in diabetic bio-models. Int J Biol Macromol. 2024;254:127691.
19. Li S, Guo W, Zhang M, Zeng M, Wu H. Microalgae polysaccharides exert antioxidant and anti-inflammatory protective effects on human intestinal epithelial cells in vitro and dextran sodium sulfate-induced mouse colitis in vivo. Int J Biol Macromol. 2024;254:127811.
20. Zhang D, et al. Oral Microalgae-Nano integrated system against Radiation-Induced injury. ACS Nano. 2023;17:10560–76.
21. Rao A, Briskey D, Nalley JO, Ganuza E. Omega-3 Eicosapentaenoic Acid (EPA) Rich Extract from the Microalga Nannochloropsis Decreases Cholesterol in Healthy Individuals: A Double-Blind, Randomized, Placebo-Controlled, Three-Month Supplementation Study. Nutrients. 2020;12:1869.
22. Davinelli S, Nielsen ME, Scapagnini G. Astaxanthin in skin health, repair, and disease: A comprehensive review. Nutrients. 2018;10:522.
23. Donoso A, González-Durán J, Muñoz AA, González PA, Agurto-Muñoz C. Therapeutic uses of natural Astaxanthin: an evidence-based review focused on human clinical trials. Pharmacol Res. 2021;166:105479.
24. Sun X, et al. A tumor microenvironment-activatable nanoplatform with phycocyanin-assisted in-situ nanoagent generation for synergistic treatment of colorectal cancer. Biomaterials. 2023;301:122263.
25. Pan R, et al. Spirulina phycocyanin induces differential protein expression and apoptosis in SKOV-3 cells. Int J Biol Macromol. 2015;81:951–9.
26. Almomani F, Bhosale RR. Bio-sorption of toxic metals from industrial wastewater by algae strains Spirulina platensis and Chlorella vulgaris: application of isotherm, kinetic models and process optimization. Sci Total Environ. 2021;755:142654.
27. Zhao G, et al. Assessment of efficacy and safety by callispheres versus hepaspheres for drug-eluting bead transarterial chemoembolization in unresectable large hepatocellular carcinoma patients. Drug Deliv. 2021;28:1356–62.
28. Wang D, Rao W. Bench-to-bedside development of multifunctional flexible embolic agents. Theranostics. 2023;13:2114–39.
29. Khalilov R, et al. Interactions of nanoparticles and biological systems. ABES. 2024;9:311–8.
30. Ahmadian E, et al. Anti-cancer effects of Citalopram on hepatocellular carcinoma cells occur via cytochrome C release and the activation of NF-kB. Anticancer Agents Med Chem. 2017;17:1570–7.
31. Yamasaki T, et al. A novel transcatheter arterial infusion chemotherapy using Iodized oil and degradable starch microspheres for hepatocellular carcinoma: a prospective randomized trial. J Gastroenterol. 2011;46:359–66.
32. Dong Z, et al. Progress of gelatin-based microspheres (GMSs) as delivery vehicles of drug and cell. Mater Sci Engineering: C. 2021;122:111949.
33. Cai Q-W, et al. Fabrication and flow characteristics of monodisperse bullet-shaped microparticles with controllable structures. Chem Eng J. 2019;370:925–37.
34. Luo Y, et al. Shape-Anisotropic microembolics generated by microfluidic synthesis for transarterial embolization treatment. Adv Healthc Mater. 2022;11:e2102281.
35. Liu J, et al. Polymersome-stabilized doxorubicin-lipiodol emulsions for high-efficacy chemoembolization therapy. J Control Release. 2022;350:122–31.
36. Nasibova. The modern perspectives of nanomaterial applications in cancer treatment and drug delivery. ABES. 2024;9:330–7.
37. Huseynov E, et al. Novel nanomaterials for hepatobiliary diseases treatment and future perspectives. ABES. 2024;9:81–91.
38. Li J, et al. Hepatocellular carcinoma: Intra-arterial delivery of Doxorubicin-loaded Hollow gold nanospheres for photothermal Ablation-Chemoembolization therapy in rats. Radiology. 2016;281:427–35.
39. Cheng R, et al. A pH-Responsive cluster Metal-Organic framework nanoparticle for enhanced tumor accumulation and antitumor effect. Adv Mater. 2022;34:e2203915.
40. Icard P, et al. How the Warburg effect supports aggressiveness and drug resistance of cancer cells? Drug Resist Updat. 2018;38:1–11.
41. Cheng H, et al. Extracellular acidosis restricts one-carbon metabolism and preserves T cell stemness. Nat Metab. 2023;5:314–30.
42. Gaggero S, et al. IL-2 is inactivated by the acidic pH environment of tumors enabling engineering of a pH-selective Mutein. Sci Immunol. 2022;7:eade5686.
43. Wu H, et al. Effects of environmental pH on macrophage polarization and osteoimmunomodulation. ACS Biomater Sci Eng. 2019;5:5548–57.
44. Su Y, et al. PLGA-based biodegradable microspheres in drug delivery: recent advances in research and application. Drug Delivery. 2021;28:1397–418.
45. Wu L, et al. Tumor aerobic Glycolysis confers immune evasion through modulating sensitivity to T cell-mediated bystander killing via TNF-α. Cell Metab. 2023;35:1580–e15969.
46. Végran F, Boidot R, Michiels C, Sonveaux P, Feron O. Lactate influx through the endothelial cell monocarboxylate transporter MCT1 supports an NF-κB/IL-8 pathway that drives tumor angiogenesis. Cancer Res. 2011;71:2550–60.
47. Apostolova P, Pearce EL. Lactic acid and lactate: revisiting the physiological roles in the tumor microenvironment. Trends Immunol. 2022;43:969–77.
48. Cappellesso F, et al. Targeting the bicarbonate transporter SLC4A4 overcomes immunosuppression and immunotherapy resistance in pancreatic cancer. Nat Cancer. 2022;3:1464–83.
49. Dong Z et al. Tumor Microenvironment Modulating $CaCO_3$-Based Colloidosomal Microreactors Can Generally Reinforce Cancer Immunotherapy. Adv Mater. 2023:e2308254.
50. Zhang J, et al. Arginine supplementation targeting tumor-Killing immune cells reconstructs the tumor microenvironment and enhances the antitumor immune response. ACS Nano. 2022;16:12964–78.
51. Zhang A, et al. $CaCO_3$-Encapuslated microspheres for enhanced transhepatic arterial embolization treatment of hepatocellular carcinoma. Adv Healthc Mater. 2021;10:e2100748.
52. Rosero-Chasoy G, et al. Growth kinetics and quantification of carbohydrate, protein, lipids, and chlorophyll of Spirulina platensis under aqueous conditions using different carbon and nitrogen sources. Bioresour Technol. 2022;346:126456.
53. Jiang L, et al. Phycocyanin: A potential drug for Cancer treatment. J Cancer. 2017;8:3416–29.
54. Ashaolu TJ, et al. Phycocyanin, a super functional ingredient from algae; properties, purification characterization, and applications. Int J Biol Macromol. 2021;193:2320–31.

Publisher's note